3 Synthesis and Characterization of $SrCeO_3$

3.1 Introduction

Growing global demands on supply of fuels stimulate extensive investigations towards sustainable energy sources and more efficient energy converting methods. Fuel cells exhibit by far higher efficiency than internal combustion engines and therefore attract worldwide attention as promising chemical-to-electrical energy transformation devices. Solid oxide fuel cells (SOFC) are considered as one of the most promising type of fuel cells for stationary, combined heat and power and also automotive applications, as they can be operated with wide range of fuels are resistant to poisoning by CO and H_2S and do not require expensive noble metals as electrodes [13, 191]. Most of profits and also disadvantages of SOFC (mainly due to component degradation), stem from the fact that operating temperature is relatively high, typically in the range of 600 – 1000°C. This type of fuel cell usually consists of Ni- yttrium stabilized zirconia composite as anode, $(LaSr)MnO_3$ or $(LaSr)(Co,Fe)O_3$ as cathode, and yttrium stabilized zirconia, gadolinium doped ceria, or other oxygen conducting material as solid electrolyte [192, 193]

In the last two decades, perovskite oxide $SrCeO_3$ has attracted considerable attention due to its potential applications in fuel cell, hydrogen sensor, H2–D2 gas cell, etc. [13,191-193]. Recently it has been investigated as thermal barrier coating candidate for high-temperature applications [194]. It is well known that doped $SrCeO_3$ materials show protonic conduction at elevated temperature under hydrogen-containing atmosphere, which can be used in many electrochemical processes such as hydrogen production, hydrogen sensors, etc. [195-199]. Recently composite electrolytes based on $SrCeO_3$ with high ionic conductivities have been explored for the intermediate temperature fuel cells (ITFCs) [200-202]. Moreover, like other ABO_3 oxide, $SrCeO_3$ can be oxygen deficient (by generation of oxygen vacancies) and oxygen excess (by oxygen interstitial). Oxygen ion migrates via mechanism associated with either

oxygen vacancies or oxygen interstitials. Therefore, it is considered to synthesis $SrCeO_3$ and studies structural, electrical and photo luminescent properties.

3.2 Experimental

Powder of $SrCeO_3$ was synthesized via the solid state reaction method using $SrCO_3$ (purity of 99.9%, Alfa Aesar) and CeO_2 as raw materials. CeO_2 was obtained by decomposing ammonium cerium nitrate $(NH_4)_2Ce(NO_3)_6$ (purity of 99.5%, Alfa Aesar) at 1000 °C. Stoichiometric amounts of raw materials together with a known amount of acetone (as mixing media) were milled in a planetary ball-mill (Retsch PM200, Germany) using zirconia balls for 8 h at 200 rpm. The mixtures were dried by keeping them in an oven for overnight. Thermogravimetric (TG) and differential scanning calorimetry (DSC) curves of mixtures were recorded using simultaneous TG-DSC thermal analyser (Mettler Toledo, Germany), in the temperature range of 30–1000 °C, with a heating rate of 10 °C /min in a nitrogen atmosphere. The dried mixtures were calcined in alumina crucibles at different temperatures and time to obtain phase pure powder of desire compounds. Based on the results of TG, the lowest temperature of calcination was decided at 800 °C and time of 8 h. Finally, single phase powder of $SrCeO_3$ was obtained by calcination at 1000 °C for 14 h. Obtained pure phase powders were mixed with 2 wt% polyvinyl alcohol (PVA) and pressed uniaxial into cylindrical pellets (diameter ~12 mm, thickness ~2 mm) under a load of 5 t using a hydraulic press. These pellets were kept in alumina crucibles and sintered at 1200 °C for 12 h in a high-temperature programmable muffle furnace (Matrix, India). Initially, pellets were heated slowly at a rate of 2 °C /min up to 200 °C and maintained at this temperature for 2 h to burn off the binder. The pellets were then heated at a rate of 5 °C/min to the sintering temperature of 1200 °C and kept at this temperature for 12 h. After sintering, the pellets were cooled to 600 °C at a rate of 5 °C/min followed by natural cooling up to room temperature and kept in a desiccator.

3.3 Results and Discussions

3.3.1 Thermal Analysis (TGA-DSC) of mixture of raw material

To ensure the temperature required for the reaction between raw materials to form desire compounds, thermogravimetric (TGA) and DSC measurements were carried out. TGA and DSC data of ball milled mixtures of raw materials $SrCO_3$ and CeO2 for $SrCeO_3$ (1 mole: 1 mole) were recorded up to 1000 ℃ with a heating rate of 10 ℃/min in N2 gas atmosphere. TGA and DSC curves of mixture for $SrCeO_3$ and Sr2CeO4 are shown in **Figure 3.1**. The TG curves show total weight loss approximately 14.48% (for $SrCeO_3$) in the following steps. The first step weight loss observed in the temperature range of 30–100 ℃ may be due to evaporation of remaining acetone or moisture adsorbed on the surface of the particles of the reactants. The second and main weight loss step recorded in the temperature range of 800–970 ℃ is assigned to the expulsion of CO_2 gas during reaction between $SrCO_3$ and CeO_2 according to **Eqn. (3.1)**:

$$SrCO_3 + CeO_2 \xrightarrow{yield} SrCeO_3 + CO_2 \quad (3.1)$$

The theoretically calculated weight losses for reactions (3.1) is approximately 13.76%. The theoretical and experimental percentage weight losses (in the second step) are approximately the same for the mixtures and ensure complete expulsion of CO_2 from the product.

In the DSC curve of the mixtures for $SrCeO_3$, endothermic peaks at 900 was recorded. Endothermic peaks in the DSC curves may be associated with the formation of desire compounds $SrCeO_3$ according to the reactions (3.1). The results obtained by the present work are in agreement with previously reported results [203, 204].

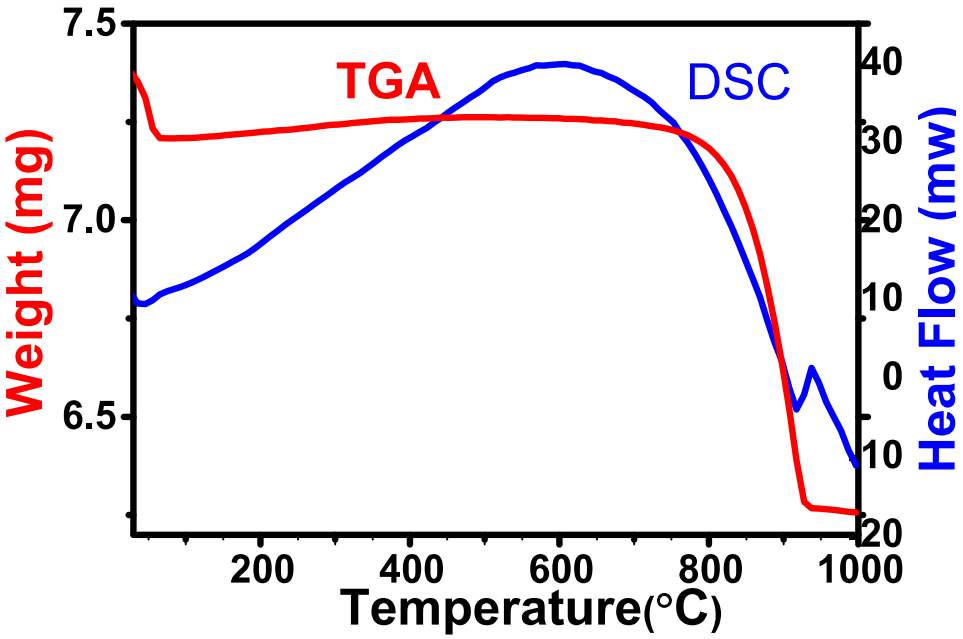

Figure 3.1 TGA-DSC curve of stoichiometric mixture of raw materials ($SrCO_3$ and CeO_2) for $SrCeO_3$.

3.3.2 Structural characterization using XRD

Powder X-ray diffraction (XRD) pattern of the mixtures for $SrCeO_3$ calcined at 900 °C for 6 h but no single phase formation obtained thereafter recalcined at 1000 °C for 14 h, got monophasic nature which is shown in **Figure 3.2(a)**. All the peaks present in the diffraction patterns were indexed to orthorhombic structure of $SrCeO_3$ (JCPDS card No. 47-1687). No peaks corresponding to any impurity phase, intermediate phase and raw materials were seen in the XRD patterns, which confirmed formation of single-phase powder of the sample.

It has been reported that the presence of impurity phases such as Sr_2CeO_4, $SrCO_3$ and CeO_2 in trace amount is unavoidable in the powder of $SrCeO_3$ synthesized by any methods. Synthesizing hundred percent pure phase powder of $SrCeO_3$ is challenging even till date. Detection of the impurity phase Sr_2CeO_4 using XRD technique is difficult because of the similarity in the XRD pattern of $SrCeO_3$ and Sr_2CeO_4 (see **Figure 3.3 (a)**).

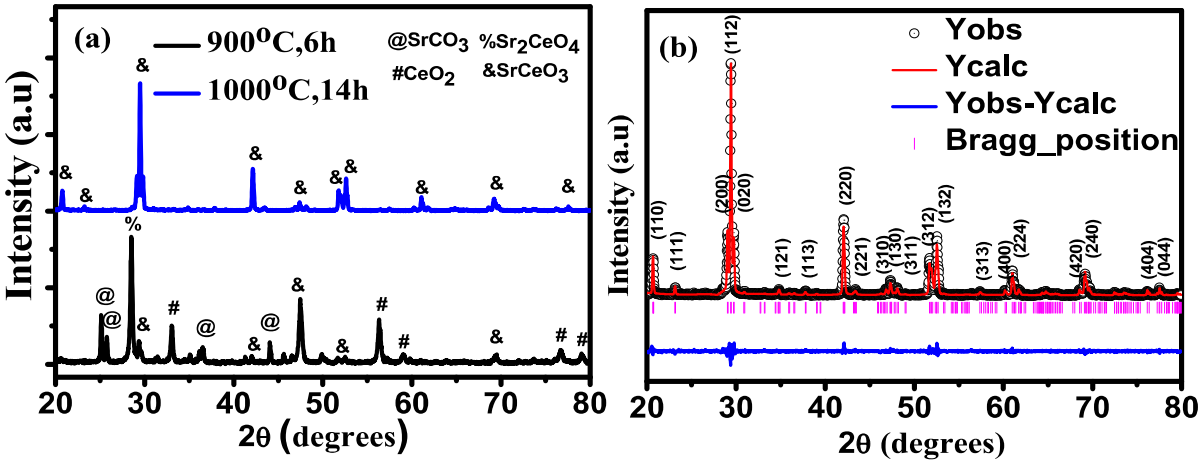

Figure 3.2 (a) XRD pattern of calcined powder and **(b)** Rietveld refinement profiles of sintered powder of $SrCeO_3$.

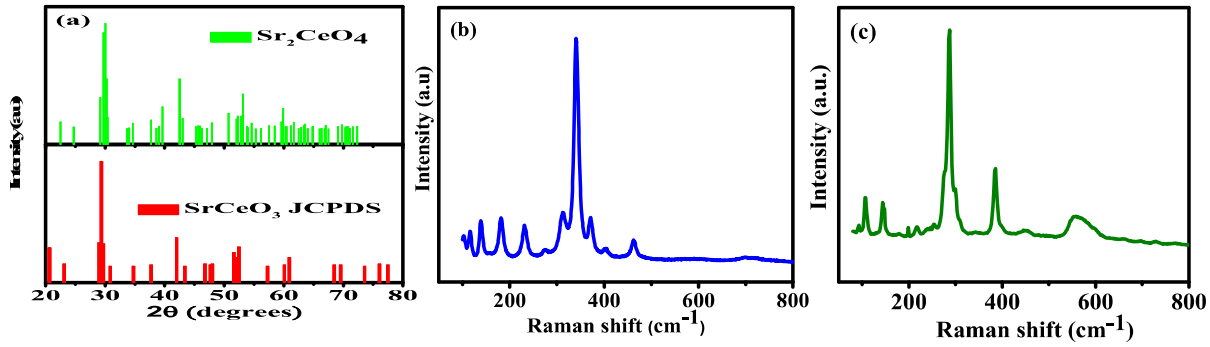

Figure 3.3 (a) JCPDS cards for $SrCeO_3$ & Sr_2CeO_4 and **(b)-(c)** Raman spectra for $SrCeO_3$ & Sr_2CeO_4 respectively.

It has been noticed from the literature survey that the Raman spectra of $SrCeO_3$ and Sr_2CeO_4 is completely different. Moreover, Raman spectroscopy can detect lower concentrations of impurity phases and is more sensitive than XRD. Therefore, to check the purity of the synthesized powders, room temperature Raman spectra in the wave number range 50–800 cm-1 has been recorded (see **Figure 3.3 (a)-(b)**). The most intense Raman band in the spectrum of sample appears at 339.51 cm-1.Other than this intense band two satellite bands at

369.46 and 313.36 cm-1 are also seen in the spectrum of the sample. The spectrum and position of various bands observed for $SrCeO_3$ synthesized in this work are in agreement with the Raman spectra recorded by earlier workers. This result confirms the formation of high purity powder of $SrCeO_3$.

For microstructural and electrical characterizations, single phase calcined powders were pelletized and sintered at 1200 °C for 12 h. The XRD diffraction pattern of sintered powders was recorded and shown in **Figure 3.2 (b)**. The XRD patterns of sintered powders and corresponding calcined powders are matching which suggest that the evolution of new phases and decomposition of $SrCeO_3$ phase did not occur during prolonging the sintering process.

Further, it was noticed that the peaks present in the XRD pattern of the sintered powders are sharper than that in the calcined powders, which confirms grain growth during sintering. The XRD pattern of sintered powders was Rietveld refined using Full-Prof software and depicted in **Figure 3.2 (b)**.

In the Rietveld refinement, the peak profiles were modelled by pseudo-Voigt function by considering six-coefficient polynomial background. The Rietveld refinement was carried out to orthorhombic crystal structure with space group Pnma. The reliability and structural parameters obtained from the refinement are listed in Table 3.1. The lattice parameters obtained from the refinement agree with the literature values [205].

The experimental density (d_{exp}) of the sintered pellets was calculated using Archimedes' principle. The theoretical density (d_{th}) of the samples was calculated from the molecular weight of the samples and their lattice parameters obtained from the Rietveld analysis. The percentage porosity of the ceramic of the samples is calculated using the formula:

$$Porosity\ (\%) = \frac{d_{th} - d_{exp}}{d_{th}} \times 100 \quad (3.2)$$

The experimental density, theoretical density and percentage porosity of the samples are mentioned in Table 3.1. It is noted from Table 3.1 that the experimental density of the sintered samples is ≥ 95% of theoretical density which confirms dense microstructure of the samples.

Table 3.1 Parameters obtained from Rietveld refinement of XRD data of $SrCeO_3$.

Space group	Pnma (62)
Crystal structure	Orthorhombic
Lattice parameter (Å)	a = 6.1312, b = 8.5604, c = 5.9946
Reliability factors	R_p = 4.3, R_{wp} = 4.1, S = R_{wp}/R_e= 0.95, χ^2 = 1.50, R_{Bragg} = 3.26
Theoretical density (gm/cm^3)	5.72
Experimental density (gm/cm^3)	5.39
Porosity (%)	5

3.3.3 Microstructural and compositional analysis

Figure 3.4 shows scanning electron micrograph (SEM) of fractured surface of pellet sintered at 1200 ℃ for 12 h. The SEM image revealed dense structure and well grown grains separated by grain boundaries. It is noted that the morphology of grains of sample is spherical and edges are smooth. The distribution in the grain size is obtained using '**ImageJ**' software and presented in the form of histogram (shown in inset of **Figure 3.4 (a)**).

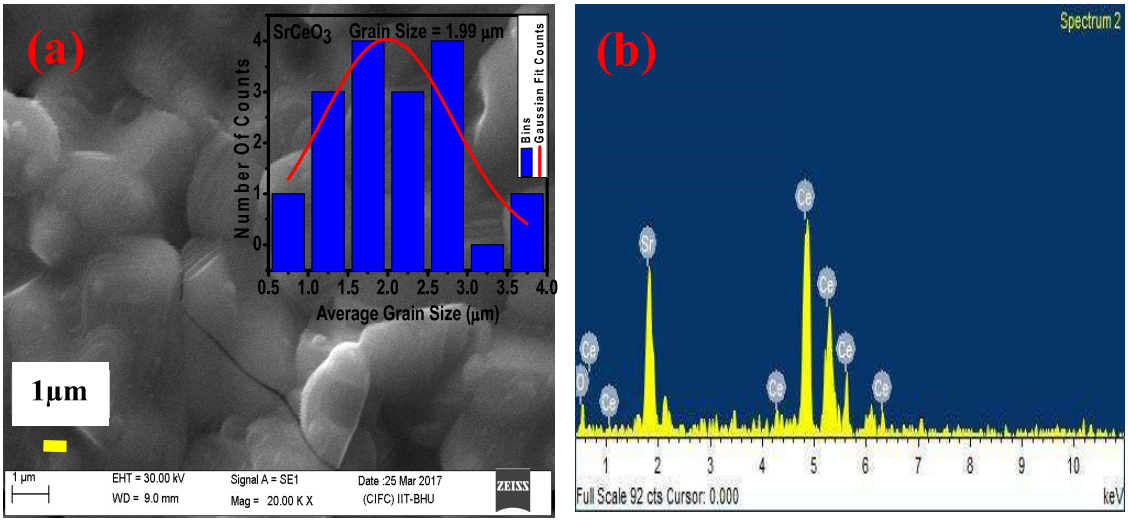

Figure 3.4 (a) SEM micrograph **(b)** EDX spectrum of fractured surface of sintered pellet.

The average value of grain size of the sample was obtained by fitting Gaussian function to the distribution of grain sizes as shown in **Figure3.4 (a)**. The average grain size of the sample is found to be 1.99 µm. The obtained value of average grain size for the compound is consistent with previous reports available in the literature on these oxides [194, 206].

Compositional homogeneity (in terms of the concentration profile of the elements) was probed by recording energy dispersive X-ray (EDX) spectrum of different regions of the fractured surface of the pellet. EDX spectrum of one of the randomly chosen regions is shown in **Figure 3.4 (b)**. **Figure 3.4 (b)** shows the presence of peaks corresponding to Sr, Ce, and O elements only. Quantitative data for atomic and weight percentage of the elements present in different regions is as per expected stoichiometry of $SrCeO_3$ ceramic.

3.4 Electrical characterization

3.4.1 By impedance spectroscopy

Complex impedance spectroscopy is a powerful technique for analysing the electrical properties of the polycrystalline materials [181]. This technique enables us to separate out the contribution of grain, grain boundary, and sample-electrode interface from the total impedance/resistance of a polycrystalline sample. Impedance data can be presented in two types of plots: (1) complex plane, e.g., Z″ (imaginary component) vs. Z′ (real component) and (2) spectroscopy such as Z″ vs. logf. Complex plane plot in general reveals information from features like curve shape and intercepts. On the other hand, the spectroscopic plots show the frequency dispersion directly including the location and width of a relaxation peak.

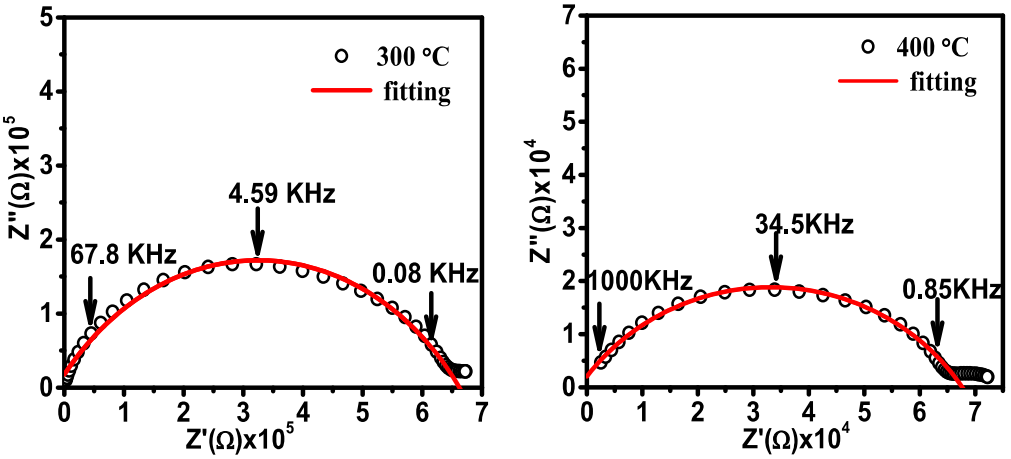

Figure 3.5 Complex plane impedance plots (Nyquist plots of the sample).

Figure 3.5 shows complex plane impedance (Nyquist) plots of prepared sample at two different temperatures. At low temperatures (< 300 °C), a straight line is seen, indicating the insulating behaviour properties of the material. In the plots at higher temperatures (≥ 300 °C), a large depressed (centre lying below the real axis) semicircular arc in the high frequency range and a small tail in the low frequency range are seen. To obtain the value of resistance (R)

corresponding to high frequency arc, the impedance data were fitted using a software by considering circle equation $\left(Z' - \frac{R}{2}\right)^2 + Z''^2 = \frac{R^2}{4}$. The corresponding capacitance (C) was calculated using the formula $\omega\tau = 2\pi f_{max} RC = 1$, f_{max} is the frequency of the maximum of the semicircle, $\omega\tau = 2\pi f_{max} RC$, and τ is the relaxation time. The value of capacitance is found to be of the order of 10^{-11} F for the sample. It is reported in Ref. [208] that the capacitance of the gains of many polycrystalline ceramic oxides lies in the range of pF ($10^{-12} - 10^{-10}$ F) while that of the grain boundaries in the range of nF ($10^{-9} - 10^{-8}$ F). Thus the obtained value of capacitance indicates that the observed high-frequency semicircle can be attributed to the electrical conduction through the bulk (i.e., grain interior).

To get more information about relaxation phenomenon, impedance data were also represented as spectroscopic plots. **Figure 3.5** shows the variation of the imaginary part of impedance (Z″) as a function of logarithm of frequency at few different temperatures. The Z″ increases with increase in frequency and reaches a maximum value before starts decreasing rapidly. The position of Z″ peak shifts towards higher frequency side with an increase in temperature suggests the existence of a temperature dependent relaxation phenomenon. The relaxation phenomenon in the samples may be due to the presence of defect species. The height of plots of Z″ against logf is proportional to the resistance according to **Eq. (3.3)** [209]:

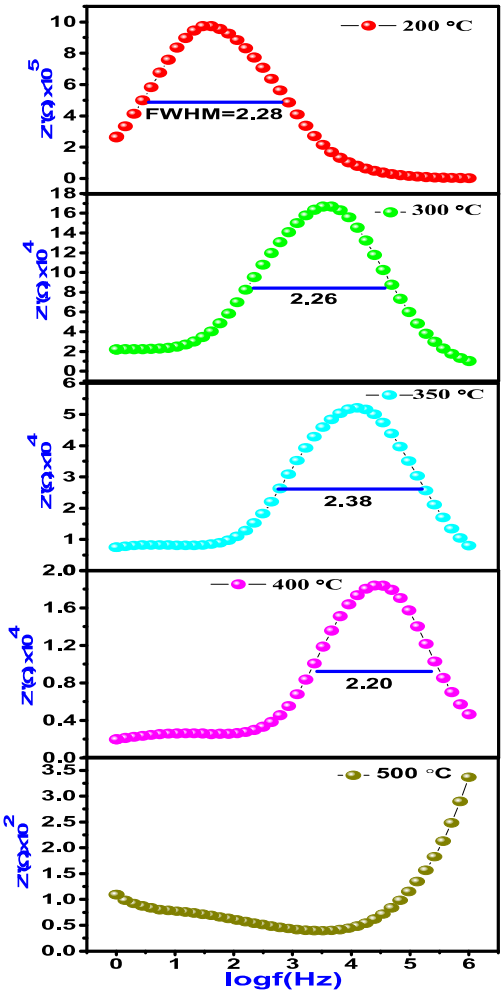

Figure 3.6 Variation of imaginary part of impedance (Z'') with logarithm of frequency at different temperatures. FWHM represents the value of the full width at half-maxima.

$$Z'' = R\,(\omega\tau/1 + \omega^2\tau^2) \tag{3.3}$$

At peak position ($\omega\tau = 1$), the height of the peak is R/2. Using this approach, values of R at different temperatures were calculated and given in Table 3.2. The corresponding relaxation frequencies (f_{relax}) and capacitances are also given in Table 3.2. Variation of R with the inverse of temperature is shown in **Figure 3.7**. Activation energy of conduction (E_{cond}) has been determined using Arrhenius relation and found to be 0.90 eV for the sample. Variation

Table 3.2 Values of relaxation frequency, resistance and capacitance evaluated from Z" Versus log (f) plots.

Temperature (°C)	**Frequency (Hz)**	**Resistance R_{total} (Ω)**	**Capacitance,C_{total}(F)**
200	41.32	19.44×10^{6}	1.98×10^{-10}
300	3279.6	32.13×10^{4}	1.51×10^{-10}
350	12,599	10.40×10^{4}	1.21×10^{-10}
400	34,572	3.66×10^{4}	1.26×10^{-10}
500	600,000	7.01×10^{3}	1.12×10^{-10}

Of $\log\tau_{relax}$ ($\tau_{relax} = 1/f_{relax}$) with the inverse of temperature is shown in **Figure 3.8**. Linear behaviour of $\log\tau_{relax}$ with 1000/T indicates that relaxation time obeys Arrhenius relation given by **Eq. (3.4)**:

$$\tau_{relax} = \tau_o exp\left(E_{relax}/K_B T\right) \quad (3.4)$$

Where τ_o is the relaxation time at infinite temperature, E_{relax} is the activation energy, K_B is the Boltzmann's constant and T is the absolute temperature. A linear fit of the $\log\tau_{relax}$ vs. 1000/T (see **Figure 3.8**) plot has been used to estimate the activation energy of relaxation process of the sample. The value of activation energy obtained from $\log\tau_{relax}$ vs. 1000/T and logR vs. 1000/T plots is the same for the sample. This result shows that mechanism of electrical conduction and relaxation in the sample is the same. In other words, the same charge specie is involved in relaxation and conduction.

The value of full width and half maxima FWHM) of the peaks shown in **Figure 3.6** is larger than 1.144 decades (for ideal Debye-type relaxation) for both the samples. This shows a presence of non-Debye nature of the relaxation phenomenon in the sample. The value of FWHM is 2.44 decades for $SrCeO_3$.

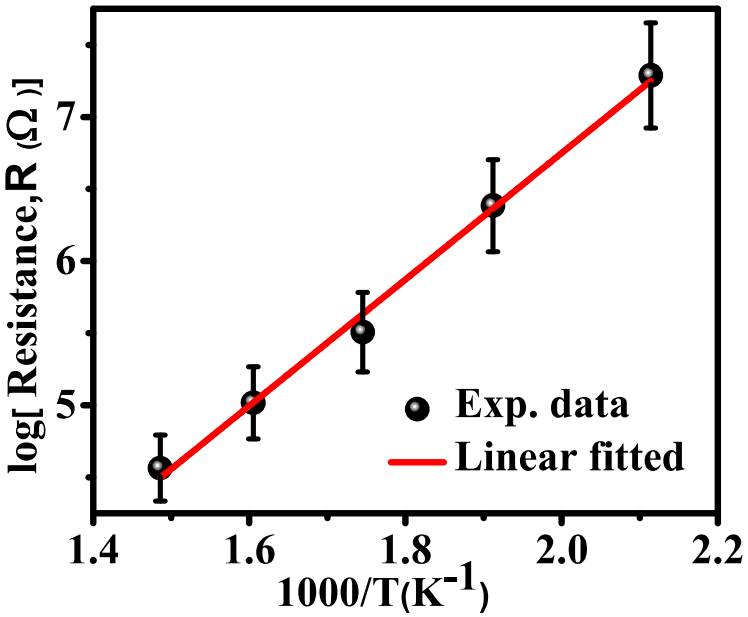

Figure 3.7 Variation of logarithm of R with inverse of temperature.

Relaxation peak may be wider either due to overlapping of two peaks /or a single peak originating from a wide distribution of relaxation time due to a variety of energy barriers resulting from local defects. In the microstructure of sample, grain boundaries are distinctly visible. Therefore, it is proposed that broad peak in the sample is due to overlapping of peak corresponding to grain and grain boundaries.

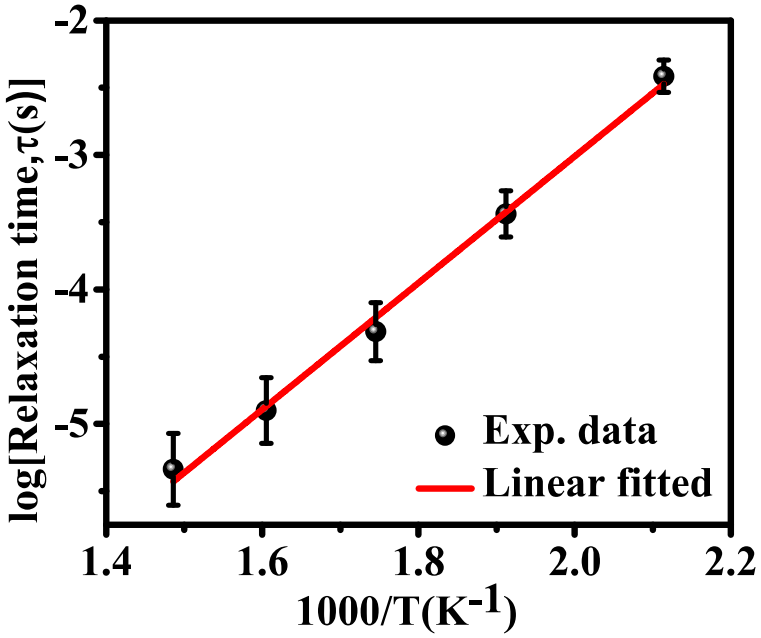

Figure 3.8 Variation of logarithm of relaxation time of grain with inverse of temperature.

3.4.2 By DC conductivity measurements

The theoretical density (d_{th}) of the sample was calculated by molecular weight of the sample and their lattice parameters obtained from the Rietveld analysis. Due to the limited range of the available multimeter and high values of the DC resistance of the sample, experimental data below 200 °C could not be collected. The DC resistances of the sample were measured in the temperature range of 200–600 °C by two-probe method. The DC conductivity (σ_{dc}) of the sample was calculated from the measured resistances and geometrical parameters (thickness and diameter) of the pellet. The plot of $\log\sigma_{dc}$ vs. 1000/T for the sample is shown in Figure 3.8. A linear variation is observed between σdc and 1000/T which confirms Arrhenius relationship given below

$$\sigma_{dc} = \sigma_o exp\left(-{}^{E_{cond}}/_{K_B T}\right) \tag{3.5}$$

Where σ_o is constant, K_B is the Boltzmann's constant and E_{cond} is the activation energy of DC conduction. The value of E_{cond} for the sample is obtained by least square fitting of the conductivity data and found to be 0.89 eV. Observed order of DC conductivity and corresponding activation energy of sample agree with earlier studies on electrical properties [38, 39]. It is well known that doubly ionized oxygen vacancy ($V_o^{\cdot\cdot}$) is the most mobile defect charge specie in the perovskite oxides and doped and undoped ceria oxides. The typical value of the activation energy for the migration of $V_o^{\cdot\cdot}$ lies in the range of 0.55–1.30 eV [210-212]. The obtained value of the activation energy for DC conduction of $SrCeO_3$ fall in this range; therefore, conduction in these sample is ascribed to the migration of doubly ionized oxygen vacancies($V_o^{\cdot\cdot}$). Formation of oxygen vacancies in these sample could have taken place during sintering at high temperature (1200 °C).

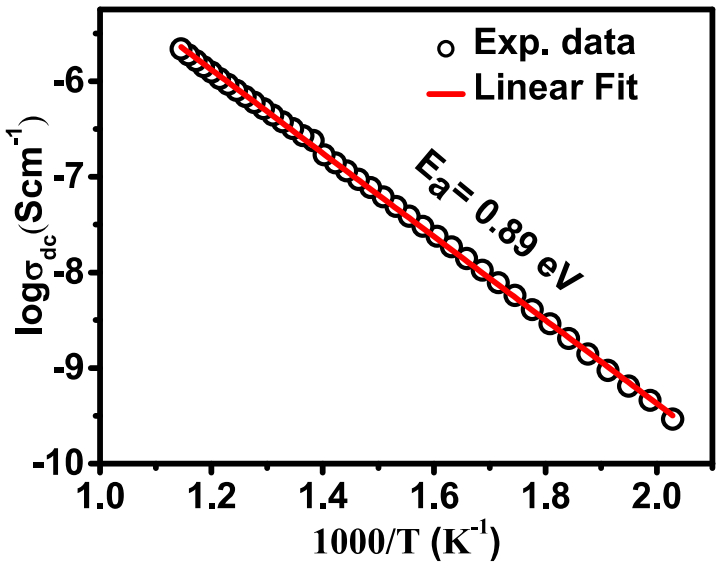

Figure 3.9 Variation of logarithm of DC conductivity (σ_{dc}) with inverse of temperature.

The value of activation energy obtained from **Figure 3.7** and **3.8** when compared with the value of activation energy obtained from DC conductivity measurement **(Figure 3.9**) is seen to have the same value within the experimental error for the sample. The same value of the activation energy from the methods suggest that bulk contribution is dominating in electrical conduction; contribution of grain boundaries and the electrode-ceramic interface is almost negligible. Further, the activation energy value suggest that the relaxation process and conduction mechanism in the sample are of similar source.

3.4.3 Photoluminescence studies

Presence of oxygen vacancies in various oxides have been revealed by measuring PL properties [213]. PL emission spectra of the sample was recorded (exciting with a source of wavelength 280 nm) which are shown in **Figure 3.10**. PL spectra of $SrCeO_3$ were compared with spectra of Sm^{3+} doped $SrCeO_3$ [214]. The emission peak of $SrCeO_3$ was deconvoluted into three peaks centred at 441 nm (2.81 eV), 462 nm (2.69 eV) and 502 nm (2.47 eV) as shown in **Figure 3.10**. Based on Ref. [213] peak 1 and 2 are the characteristic emission peaks while peak 3 is assigned to the presence of defect, i.e. oxygen vacancies. Various authors have ascribed the peak around 520 nm (2.40 eV) to the energy level of doubly ionized oxygen vacancies [213].

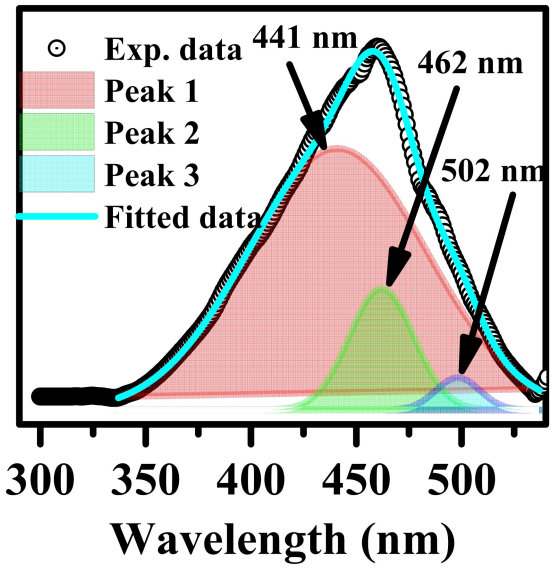

Figure 3.10 Emission spectrum of sintered sample.

3.5 Conclusions

The Rietveld refinement of XRD data of sintered powder confirmed orthorhombic structure and space group Pnma. SEM studies indicated that the compound has dense microstructure. Impedance analysis confirmed presence of single non-Debye type relaxation phenomena in the sample. The activation energy for relaxation time (E_{relax}) and the activation energy for DC conduction (E_{cond}) is the same for the sample. Based on the numerical value of activation energies, relaxation and conduction mechanism in the compound are assigned to migration of doubly ionized oxygen vacancies($V_o^{\cdot\cdot}$). PL technique confirmed presence of oxygen vacancies in the compound.